An extremely bright gamma-ray pulsar in the Large Magellanic Cloud

The Fermi LAT collaboration*

*The full list of authors is at the end of the paper.

Pulsars are rapidly spinning, highly magnetized neutron stars, created in the gravitational collapse of massive stars. We report the detection of pulsed GeV gamma rays from the young pulsar PSR J0540−6919 in the Large Magellanic Cloud, a satellite galaxy of the Milky Way. This is the first gamma-ray pulsar detected in another galaxy. It has the most luminous pulsed gamma-ray emission yet observed, exceeding the Crab pulsar's by a factor of twenty. PSR J0540−6919 presents an extreme test case for understanding the structure and evolution of neutron star magnetospheres.

The first pulsar was discovered in 1967 as a puzzling celestial source of periodic radio pulses. Nearly 2500 pulsars have since been detected, mostly in the Milky Way but also in other nearby galaxies, and their characteristic pulsed emission has been observed across the electromagnetic spectrum. The energy source for emission from pulsars is the rotation of a magnetized neutron star. The mechanism is radiation by particles accelerated by intense electric fields in the neutron star magnetosphere. The pulsar spins with period P, and the observed rate at which it slows down $\frac{dP}{dt} = \dot{P}$ sets the scale of the power reservoir for particle acceleration and emission processes. Spin-down power is $\dot{E} = 4\pi^2 I\dot{P}/P^3$, where I denotes the neutron star moment of inertia, taken to be 10^{45} g cm^2 (*1*), which roughly corresponds to a solid sphere of

10 km radius and the mass of the Sun.

The Large Area Telescope (LAT), an imaging instrument on the *Fermi* satellite sensitive to gamma rays with energies 20 MeV–300 GeV (*2*), has detected gamma-ray pulsations from over 160 pulsars (see the second *Fermi*-LAT pulsar catalog (*3*), and the public list of LAT-detected gamma-ray pulsars (*4*)). Gamma-ray pulsars have $\dot{E} > 10^{33}$ erg s^{-1}, and a significant fraction (>30% in many cases) of their spin-down power is converted into gamma-ray luminosity L_γ. In contrast, radio emission represents a negligible fraction of the total energy output (*3*). Gamma-ray observations thus probe the sites and processes of particle acceleration and radiation in pulsars. Candidate emission regions range across the magnetosphere out to the "light cylinder", where co-rotation with the neutron star would reach the speed of light (*5–7*). In these regions, curvature or synchrotron radiation from accelerated electrons initiates electromagnetic cascades by interacting with the strong magnetic field or with ambient photons; the electron-positron pairs produced are accelerated and radiate in turn, giving rise to further pairs. Emission may also originate in the pulsar's plasma wind, beyond the light cylinder (*8*).

Discriminating between emission scenarios requires spectra and light curves in various wavebands for pulsars with different ages, magnetic field strengths, and viewing geometries. Few pulsars younger than several thousand years are known. The pulsar in the Crab supernova remnant is the best studied and was the most powerful known in pulsed gamma rays (*9*). The Crab pulsar has $\dot{E} = 4.5 \times 10^{38}$ erg s^{-1}. Only one known pulsar has a larger spin-down power, PSR J0537$-$6910 with $\dot{E} = 4.9 \times 10^{38}$ erg s^{-1}, whilst PSR J0540$-$6919, only 16 arcmin away, has the third highest $\dot{E} = 1.5 \times 10^{38}$ erg s^{-1}. Both of the latter are located in the Large Magellanic Cloud (LMC), a satellite galaxy of the Milky Way at a distance $d \sim 50$ kpc (*10*). PSR J0537$-$6910 is a 16-ms pulsar associated with the ~5000-year old supernova remnant LHA 120-N 157B (*11,12*), while PSR J0540$-$6919 is a 50-ms pulsar associated with the ~1140-year old supernova remnant SNR 0540-69.3 (*13–15*). Although these two pulsars are of comparable age and energetics, their gamma-ray behavior appears to be markedly different. This paper reports the detection of gamma-ray pulsations from PSR J0540−6919 and an upper limit on gamma-ray pulsations from PSR J0537−6910.

Fermi-LAT predominantly operates in all-sky survey mode; hence the LMC has been observed regularly since launch. Gamma-ray emission from the LMC is particularly prominent near the Tarantula nebula (30 Doradus) (*16*), a very active star-forming region hosting extremely massive stars (*17, 18*). PSR J0537−6910 and PSR J0540−6919 lie in this area, but until now neither could be identified as discrete gamma-ray sources. Now, over six times more data are available compared to the earlier *Fermi*-LAT study (*16*), and the recent revision of LAT event reconstruction, called Pass 8, significantly enhanced the sensitivity of LAT data analyses (*19*). We thus revisited the gamma-ray emission from the LMC, and the 30 Doradus region in particular.

We analyzed Pass 8 events from 75 months of *Fermi*-LAT all-sky survey observations (*43*). The gamma-ray emission from the LMC is shown in Figure 1, after subtracting fitted models of the Galactic foreground emission, an isotropic background, and point-like sources outside the LMC. The improved angular resolution with increasing gamma-ray energy makes two point-like sources coincident with the pulsars stand out above 2 GeV.

The source coincident with PSR J0540−6919 is detected with a statistical significance of 17σ. Its photon spectrum is well described by a power law with exponential cutoff, typical of gamma-ray pulsars (*3*). To search for pulsations, we built a rotation ephemeris using Rossi X-ray Timing Explorer (RXTE) (*20*) observations recorded between modified Julian day 54602 (2008 May 16) and 55898 (2011 December 3), shortly before the end of the RXTE mission (see Table S1). We phase-folded the gamma-ray data from the first 3.5 years of the *Fermi* mission corresponding to the ephemeris. We used the LMC emission model to assign each photon the probability that it originated from PSR J0540−6919, based on reconstructed positions and energies and the instrument response functions (*21*). Figure 2 shows the probability-weighted

$E >$100 MeV gamma-ray pulse profile for probabilities > 0.1. The weighted H-test parameter (*21, 22*) is 63.5, corresponding to a significance of 6.8σ, making this the first extragalactic gamma-ray pulsar.

Time-averaged gamma-ray emission from the source coincident with PSR J0537$-$6910 is detected with significance 11σ. Its spectrum is consistent with a simple power law with photon index 2.1 ± 0.1 extending to > 50 GeV without evidence for a cutoff. A weighted phase-fold of the LAT data based on an RXTE ephemeris limited any pulsed emission to significance $< 1\sigma$ (see Table S2). The 95% confidence level upper limit on the 0.1–10 GeV pulsed luminosity for this pulsar is 1.9×10^{35} erg s^{-1}. This and the lack of a spectral cutoff suggest that strongly pulsed emission is at most a small fraction of the total signal from the source. The gamma-ray signal may instead result from the superposition of weakly modulated pulsar emission and radiation from the pulsar wind nebula and the supernova remnant, in unknown proportions.

Figure 2 also shows the X-ray pulse profile for PSR J0540$-$6919, obtained by integrating all the RXTE data used to build the timing solution. The profile matches previous results (*23*). The optical light curve was evaluated using the RXTE ephemeris to fold data from the Iqueye photometer mounted on the ESO 3.6-m New Technology Telescope (NTT) in January and December 2009 (*24*). We also show a radio profile formed from the sum of 18 bright giant pulses recorded at the Parkes telescope at 1.4 GHz in August 2003 (*25*). Emission components from radio to gamma rays are aligned, but the shape of the pulse varies over the different bands. The radio profile exhibits two narrow peaks separated by $\Delta \sim 0.25$ in pulse phase. This double-peak pattern is still visible on top of a broader component in the optical profile. Structures in the X-ray and perhaps gamma-ray profiles are reminiscent of the double radio peaks separated by $\Delta \sim 0.25$, but both profiles are consistent with a single bump spanning the interval between the radio peaks. In outer-magnetosphere models, the pulse peak profiles are sensitive to the magnetic geometry. In the classical vacuum ‘outer gap’ model (*5*), pulse separations as small

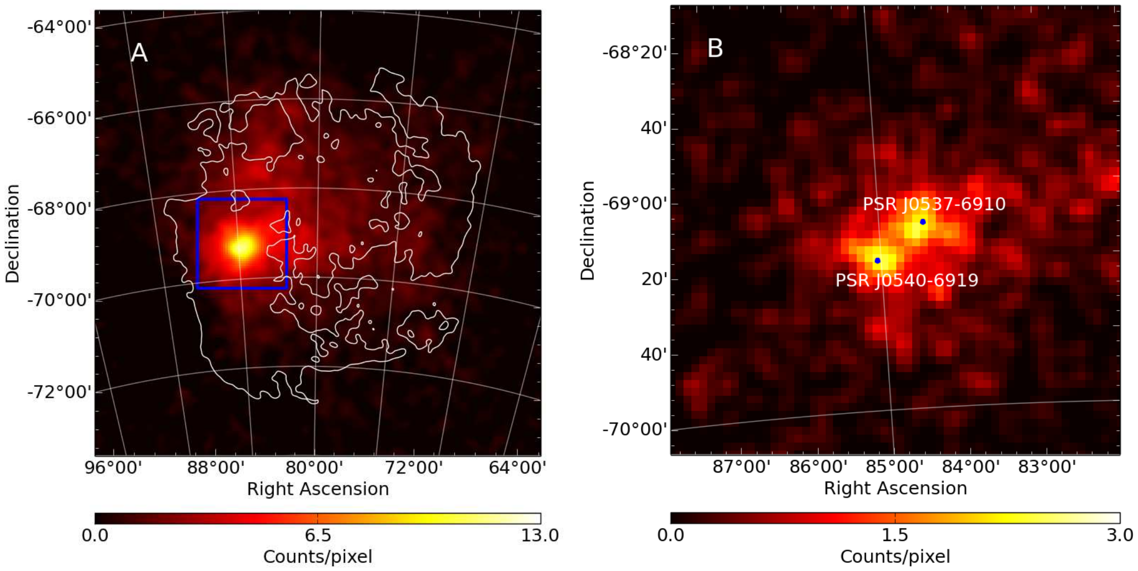

Figure 1: **Sky maps of the LMC.** (A) 0.2–200 GeV gamma-ray emission in a $10^\circ \times 10^\circ$ region encompassing the LMC. The map was smoothed using a Gaussian kernel with $\sigma = 0.2^\circ$. Emission is strongest around 30 Doradus (approximately delimited by the blue box), but also fills much of the galaxy. Contours show the atomic gas distribution. (B) 2–200 GeV gamma-ray emission in a $2^\circ \times 2^\circ$ region around 30 Doradus. The map was smoothed using a Gaussian kernel with $\sigma = 0.1^\circ$. Better angular resolution at higher energies resolves two components coincident with PSR J0540$-$6919 and PSR J0537$-$6910, whose locations are indicated as blue dots. Both maps are given in J2000 equatorial coordinates.

as $\Delta = 0.25$ occur for high $\dot{E}$, narrow-gap pulsars when the spin-axis viewing angle ζ is $> 80^\circ$ and the magnetic inclination α is $< 30^\circ$ (*26*). Models with partly resistive magnetospheres and emission extending beyond the light cylinder point to $\zeta \approx 60^\circ$ and $\alpha \approx 30^\circ$, but differing resistivity prescriptions may allow larger ζ (*7*). For such geometry, the low-altitude classical radio emission would not be observable, leaving only the high-altitude giant pulse component.

The signal above the background estimate in Figure 2 suggests a steady component of the gamma-ray emission from the direction of PSR J0540$-$6919. Likelihood analysis of the data in the off-pulse phase interval 0.3–0.8 shows a significant ($\sim 5\sigma$) point source at the position of PSR J0540$-$6919. The spectrum is consistent with that of the full phase interval, but may

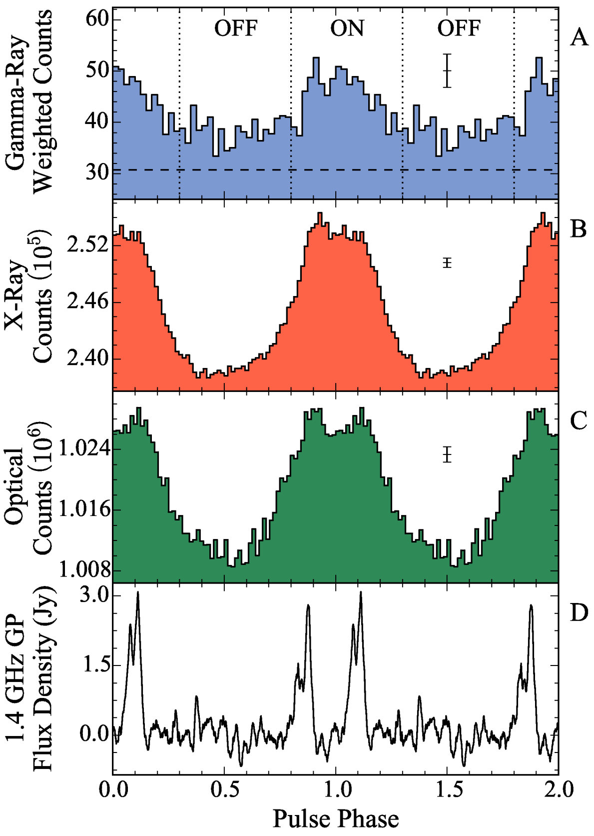

Figure 2: **Pulse profiles for PSR J0540$-$6919.** (A) Probability-weighted LAT count profile. The horizontal dashed line approximates the background level. Vertical lines indicate the on- and off-pulse regions used for the LAT spectral analysis. (B) RXTE X-ray integrated count profile. (C) NTT optical count profile. (D) Parkes radio flux profile from summing 18 bright giant radio pulses at 1.4 GHz. Two complete cycles are shown. The error bars in the top three panels represent the median phase bin errors.

be almost as well described by a single power law (see Figure S1). We cannot currently distinguish whether this represents an unpulsed magnetospheric component, emission from the associated pulsar wind nebula LHA 120-N 158A or from the surrounding supernova remnant SNR 0540$-$69.3, or residual emission from the LMC itself. Comparing with the flux in the on-pulse phase interval, we estimate that the pulsed component is $\approx$75% of the total. The choice of the off-pulse phase interval, hence the unpulsed flux estimate, is conservative because it clearly includes pulsed optical and X-ray emission (see Figure 2).

Figure 3 shows the phase-averaged spectrum of PSR J0540$-$6919. The photon spectrum is well described by a power law with photon index $2.2{\pm}0.1$ and exponential cutoff at $E_{\rm cut} = 7.5{\pm}2.6$ GeV. This photon index follows the trend of increasing index with $\dot{E}$ described in (*3*). This correlation can be explained by stronger pair formation activity in high-$\dot{E}$ pulsars, reprocessing the radiation to lower energies and leading to steep radiating particle spectra. PSR J0540$-$6919 has the second largest magnetic field at the light cylinder of any gamma-ray pulsar known, after the Crab pulsar, with $B_{\rm LC} = 4\pi^2 \left(I\dot{P}\right)^{1/2} \left(c^3 P^5\right)^{-1/2} = 3.62 \times 10^5$ G. Our $E_{\rm cut}$ measurement favors the trend of increasing cutoff energy as a function of $B_{\rm LC}$, also noted in (*3*), suggesting emission originating from the outer magnetosphere of the neutron star.

The total phase-averaged luminosity of PSR J0540$-$6919 above 100 MeV is $L_\gamma = 4\pi f_\Omega h d^2 = 7.6 \times 10^{36}\,(d/50\,{\rm kpc})^2$ erg s^{-1}, where $h = (2.6 \pm 0.3)\, \times\, 10^{-11}$ erg cm^{-2} s^{-1} is the energy flux, and the geometry-dependent beaming correction factor $f_\Omega \sim 1$ for young pulsars with the most probable viewing angle $\sim 90^\circ$ (*26*), consistent with the geometrical setting derived above. As stated above, ≈75% of the total luminosity is pulsed and may be safely attributed to the pulsar, i.e. 5.7×10^{36} erg s^{-1}. The systematic uncertainties in the spectrum and luminosity of the source due to the complete LMC emission model were found to be smaller than the statistical uncertainties (*27*). And while other pulsars' luminosities can be severely affected by distance uncertainties (e.g. 25% for the Crab pulsar), for PSR J0540$-$6919 the distance to the LMC is known to 2% accuracy (*10*).

PSR J0540$-$6919 is often called the 'Crab's twin' because they have similar magnetic field strengths, rotation rates, and ages, so a comparison is in order. The Crab pulse profile has two peaks, phase-aligned from the radio to the gamma-ray band, while PSR J0540$-$6919 has a broad gamma-ray pulse straddling the phase-range of the two narrow radio peaks, with structures in the optical and X-ray reminiscent of the radio peaks. The similarity in their radio behav-

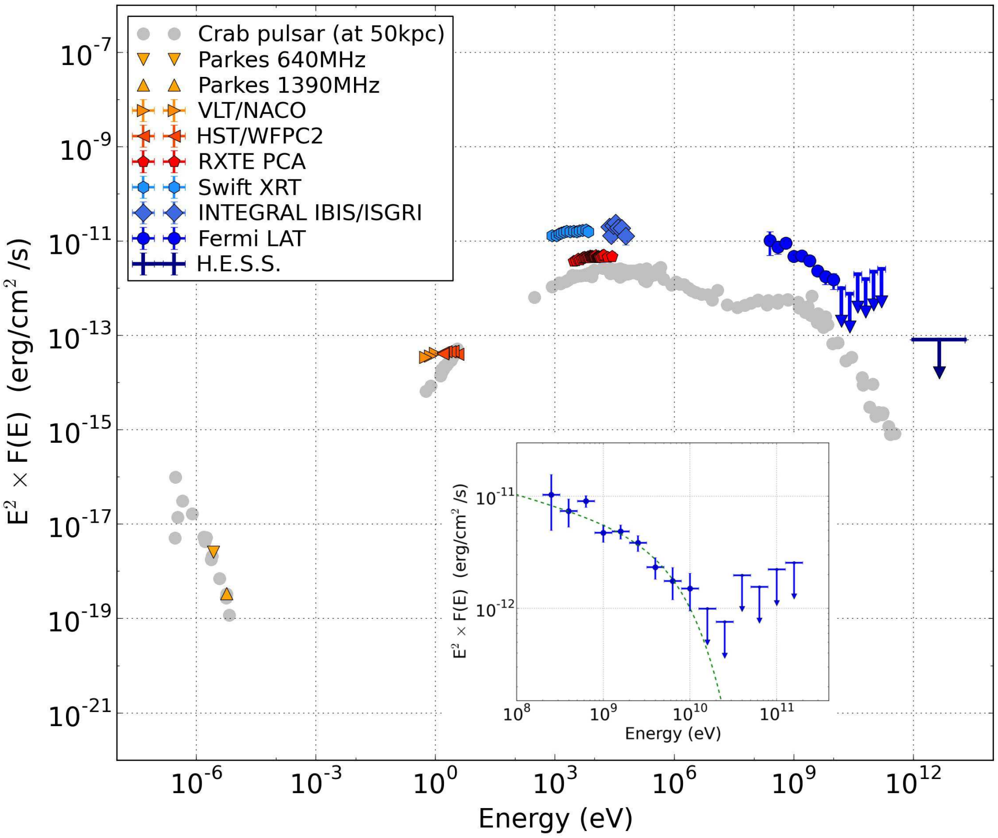

Figure 3: **Spectral energy distribution of PSR J0540−6919.** Pulsed radio data from (*25*,*28*); extinction-corrected phase-averaged near-infrared and optical fluxes from (*29*,*30*); X-ray fluxes from (*23*), including pulsed RXTE data and total spectra for the pulsar and its nebula from Swift and INTEGRAL; TeV upper limit from (*31*). The LAT data points correspond to the phase-averaged emission, which includes an estimated 25% of unpulsed emission. Crab pulsar phase-averaged data rescaled to a 50 kpc distance are shown for comparison in light grey (*9*). Inset: LAT data fit to a power law with an exponential cutoff.

ior is particularly significant, as for both pulsars the radio emission is dominated by so-called ‘giant pulses’, sporadic radio bursts with sub-microsecond durations and fluxes with a power-law distribution extending to $> 10^3$ times the average value (*32*). In (*25*) it is suggested that the co-location of the giant pulses with high-energy emission occurs in pulsars with high magnetic fields at the light cylinder, and very robust and extensive outer magnetosphere pair production.

Prior to this work, only six other pulsars showed giant pulse emission associated with strong optical, X-ray, or gamma-ray components (*33*). The discovery of gamma-ray emission from PSR J0540$-$6919 provides a new look at these rare sources.

PSR J0540$-$6919 and the Crab also share many spectral similarities, as illustrated in the radio-to-gamma-ray spectral energy distribution (Figure 3). With large powers in both pulsed X-rays and gamma rays and the absence of a strong high-energy cutoff, PSR J0540$-$6919 is similar to the Crab and unlike most middle-aged pulsars where GeV gamma-ray power dominates. Both characteristics may originate from the higher pair densities that allow synchrotron self-Compton emission to dominate and produce higher-energy pulsations. It remains to be seen whether PSR J0540$-$6919 follows the Crab in exhibiting a high-energy tail of pulsed emission, extending far above $E_{\rm cut}$ and likely attributable to inverse Compton scattering (*34, 35*). The source is currently undetected in TeV gamma rays (*31*), but may be in reach of future instruments such as the Cherenkov Telescope Array.

Yet, while the radio, optical, and X-ray luminosities of PSR J0540$-$6919 and the Crab are within a factor of $\sim$2, PSR J0540$-$6919 is much brighter in gamma rays. Its isotropic pulsed gamma-ray luminosity is about 20 times more than the Crab pulsar's, $L_\gamma = 3.2 \times 10^{35}\,(d/2\,{\rm kpc})^2\,{\rm erg\,s^{-1}}$ (*3*). PSR J0540$-$6919's pulsed luminosity remains larger than the Crab pulsar's even when including their intense X-ray emission: combining the 2–10 keV and 20–100 keV pulsed flux measurements from (*23*) gives an integrated luminosity for PSR J0540$-$6919 of $L_{X+\gamma} \sim 9.7 \times 10^{36}\,(d/50\,{\rm kpc})^2\,{\rm erg\,s^{-1}}$, while it becomes $L_{X+\gamma} \sim 2.4 \times 10^{36}\,(d/2\,{\rm kpc})\,{\rm erg\,s^{-1}}$ for the Crab (*36*).

The contrast with PSR J0537$-$6910 is even more striking: it has more than three times greater spin-down power, but its pulsed gamma-ray luminosity may be at least 30 times less than PSR J0540$-$6919's. This confirms that L_γ values can vary by more than an order-of-magnitude for a given $\dot{E}$ range (*3*). Mis-estimated distances and deviations from $f_\Omega = 1$ can account for only part of this difference. The magnetic inclination may play a significant role, beyond its effect on the beaming (*37,38*).

As mentioned above, the pulse profile of PSR J0540$-$6919 suggests a high viewing angle $\zeta > 80^\circ$ and a low magnetic inclination $\alpha < 30^\circ$. Fits to *Chandra* observations of the pulsar wind nebulae shapes of PSR J0540$-$6919 and PSR J0537$-$6910 indicate that both pulsars have similar viewing angles $\zeta \sim 90^\circ$ (*39*). In such conditions, the non-detection of radio emission from PSR J0537$-$6910 implies either a high magnetic inclination and a radio luminosity at most half that of PSR J0540$-$6919, or a misaligned radio beam, hence a low magnetic inclination similar to PSR J0540$-$6919 (*40*). The former case would confirm the role of the magnetic inclination in the observed dispersion of L_γ; the latter case would mean that the large difference in pulsed luminosity between both pulsars does not stem from different geometries. Alternatively, the non-detection of pulsations from PSR J0537$-$6910 may imply a weakly modulated gamma-ray light curve. The 'outer gap' model predicts such flat pulse profiles for $\zeta = 90^\circ$, $\alpha = 15^\circ$, and a narrow gap (*26*), a geometry quite similar to that inferred for PSR J0540$-$6919. Very similar ages, energetics, and geometries for PSR J0540$-$6919 and PSR J0537$-$6910 would therefore result in remarkable emission differences.

Our gamma-ray measurements of PSR J0540$-$6919 and PSR J0537$-$6910 offer a new look at the high-altitude accelerators in the magnetospheres of rare very young pulsars. They also have profound implications for our understanding of the high-energy emission from the LMC: $\approx$ 60% of the GeV flux density previously attributed to the 30 Doradus nebula (*16*) is now seen to be emission from PSR J0540$-$6919. With an additional ≈ 25% attributable to the source coincident with PSR J0537$-$6910, only a small fraction of the signal may originate in cosmic rays in 30 Doradus. This calls for further investigation of the relation between star-forming regions and the origin and transport of cosmic rays.

References and Notes

1. D. R. Lorimer, M. Kramer, *Handbook of Pulsar Astronomy* (2004).
2. W. B. Atwood, *et al.*, *Astrophys. J.* **697**, 1071 (2009).
3. A. A. Abdo, *et al.*, *Astrophys. J. Supp.* **208**, 17 (2013).
4. The Fermi/LAT Collaboration, *https://confluence.slac.stanford.edu/display/GLAMCOG/Public+List+of+LAT-Detected+Gamma-Ray+Pulsars* (2015).
5. K. S. Cheng, C. Ho, M. Ruderman, *Astrophys. J.* **300**, 500 (1986).
6. A. G. Muslimov, A. K. Harding, *Astrophys. J.* **606**, 1143 (2004).
7. C. Kalapotharakos, A. K. Harding, D. Kazanas, *Astrophys. J.* **793**, 97 (2014).
8. J. Pétri, *Mon. Not. R. Astron. Soc.* **412**, 1870 (2011).
9. R. Bühler, R. Blandford, *Reports on Progress in Physics* **77**, 066901 (2014).
10. G. Pietrzyński, *et al.*, *Nature* **495**, 76 (2013).
11. F. E. Marshall, E. V. Gotthelf, W. Zhang, J. Middleditch, Q. D. Wang, *Astrophys. J. Lett.* **499**, L179 (1998).
12. Y. Chen, *et al.*, *Astrophys. J.* **651**, 237 (2006).
13. F. D. Seward, F. R. Harnden, Jr., D. J. Helfand, *Astrophys. J. Lett.* **287**, L19 (1984).
14. B. J. Williams, *et al.*, *Astrophys. J.* **687**, 1054 (2008).
15. T. Brantseg, R. L. McEntaffer, L. M. Bozzetto, M. Filipovic, N. Grieves, *Astrophys. J.* **780**, 50 (2014).

16. A. A. Abdo, *et al.*, *Astron. Astrophys.* **512**, A7+ (2010).

17. P. A. Crowther, *et al.*, *Mon. Not. R. Astron. Soc.* **408**, 731 (2010).

18. N. R. Walborn, *et al.*, *Astron. Astrophys.* **564**, A40 (2014).

19. W. Atwood, *et al.*, *2012 Fermi Symposium proceedings - eConf C121028, ArXiv:1303.3514* (2013).

20. H. V. Bradt, R. E. Rothschild, J. H. Swank, *Astron. Astrophys. Supp.* **97**, 355 (1993).

21. M. Kerr, *Astrophys. J.* **732**, 38 (2011).

22. O. C. de Jager, B. C. Raubenheimer, J. W. H. Swanepoel, *Astron. Astrophys.* **221**, 180 (1989).

23. R. Campana, *et al.*, *Mon. Not. R. Astron. Soc.* **389**, 691 (2008).

24. S. Gradari, *et al.*, *Mon. Not. R. Astron. Soc.* **412**, 2689 (2011).

25. S. Johnston, R. W. Romani, F. E. Marshall, W. Zhang, *Mon. Not. R. Astron. Soc.* **355**, 31 (2004).

26. R. W. Romani, K. P. Watters, *Astrophys. J.* **714**, 810 (2010).

27. *Fermi*-LAT collaboration, *submitted to Astron. Astrophys., ArXiv:1509.06903* (2015).

28. R. N. Manchester, D. P. Mar, A. G. Lyne, V. M. Kaspi, S. Johnston, *Astrophys. J.* **403**, L29 (1993).

29. R. P. Mignani, *et al.*, *Astron. Astrophys.* **515**, A110 (2010).

30. R. P. Mignani, *et al.*, *Astron. Astrophys.* **544**, A100 (2012).

31. A. Abramowski, *et al.*, *Science* **347**, 406 (2015).

32. J. M. Cordes, N. D. R. Bhat, T. H. Hankins, M. A. McLaughlin, J. Kern, *Astrophys. J.* **612**, 375 (2004).

33. A. V. Bilous, T. T. Pennucci, P. Demorest, S. M. Ransom, *Astrophys. J.* **803**, 83 (2015).

34. VERITAS Collaboration, *et al.*, *Science* **334**, 69 (2011).

35. M. Lyutikov, N. Otte, A. McCann, *Astrophys. J.* **754**, 33 (2012).

36. R. Willingale, *et al.*, *Astron. Astrophys.* **365**, L212 (2001).

37. L. Zhang, K. S. Cheng, Z. J. Jiang, P. Leung, *Astrophys. J.* **604**, 317 (2004).

38. G. Brambilla, C. Kalapotharakos, A. K. Harding, D. Kazanas, *Astrophys. J.* **804**, 84 (2015).

39. C.-Y. Ng, R. W. Romani, *Astrophys. J.* **673**, 411 (2008).

40. F. Crawford, M. McLaughlin, S. Johnston, R. Romani, E. Sorrelgreen, *Advances in Space Research* **35**, 1181 (2005).

41. W. Cash, *Astrophys. J.* **228**, 939 (1979).

42. Q. D. Wang, E. V. Gotthelf, Y.-H. Chu, J. R. Dickel, *Astrophys. J.* **559**, 275 (2001).

43. Materials and methods are available as supplementary materials on Science Online.

Supplementary Materials

www.sciencemag.org

Materials and Methods

Figure S1

Tables S1, S2

References (41-42)

The *Fermi*-LAT Collaboration acknowledges support for LAT development, operation and data analysis from NASA and DOE (United States), CEA/Irfu and IN2P3/CNRS (France), ASI and INFN (Italy), MEXT, KEK, and JAXA (Japan), and the K.A. Wallenberg Foundation, the Swedish Research Council and the National Space Board (Sweden). Science analysis support in the operations phase from INAF (Italy) and CNES (France) is also gratefully acknowledged. *Fermi*-LAT data and analysis tools are publicly available from the Fermi Science Support Center at http://fermi.gsfc.nasa.gov/ssc/.

M. Ackermann[1], A. Albert[2], L. Baldini[3,2], J. Ballet[4], G. Barbiellini[5,6], C. Barbieri[7], D. Bastieri[8,9], R. Bellazzini[10], E. Bissaldi[11], R. Bonino[12,13], E. Bottacini[2], T. J. Brandt[14], J. Bregeon[15], P. Bruel[16], R. Buehler[1], G. A. Caliandro[2,17], R. A. Cameron[2], P. A. Caraveo[18], C. Cecchi[19,20], E. Charles[2], A. Chekhtman[21], C. C. Cheung[22], J. Chiang[2], G. Chiaro[9], S. Ciprini[23,19,24], J. Cohen-Tanugi[15], A. Cuoco[12,13], S. Cutini[23,24,19], F. D'Ammando[25,26], F. de Palma[11,27], R. Desiante[5,28], S. W. Digel[2], L. Di Venere[29], P. S. Drell[2], C. Favuzzi[29,11], S. J. Fegan[16], E. C. Ferrara[14], A. Franckowiak[2], S. Funk[30], P. Fusco[29,11], F. Gargano[11], D. Gasparrini[23,24,19], N. Giglietto[29,11], F. Giordano[29,11], G. Godfrey[2], I. A. Grenier[4], M.-H. Grondin[31], J. E. Grove[22], L. Guillemot[†32,33], S. Guiriec[14,34], K. Hagiwara[35], A. K. Harding[14], E. Hays[14], J.W. Hewitt[36,37], A. B. Hill[38,2,39], D. Horan[16], T. J. Johnson[21], J. Knödlseder[40,41], M. Kuss[10], S. Larsson[42,43], L. Latronico[12], M. Lemoine-Goumard[31], J. Li[44], L. Li[42,43], F. Longo[5,6], F. Loparco[29,11], M. N. Lovellette[22], P. Lubrano[19,20], S. Maldera[12], A. Manfreda[10], F. Marshall[†14], P. Martin[†40,41], M. Mayer[1], M. N. Mazziotta[11], P. F. Michelson[2], N. Mirabal[14,34], T. Mizuno[45], M. E. Monzani[2], A. Morselli[46], I. V. Moskalenko[2], S. Murgia[47], G. Naletto[48,49], E. Nuss[15], T. Ohsugi[45], M. Orienti[25], E. Orlando[2], D. Paneque[50,2], M. Pesce-Rollins[10,2], F. Piron[15], G. Pivato[10], T. A. Porter[2], S. Rainò[29,11], R. Rando[8,9], M. Razzano[10,51], A. Reimer[52,2], O. Reimer[52,2], T. Reposeur[31], R. W. Romani[2], P. M. Saz Parkinson[53,54], A. Schulz[1], C. Sgrò[10], E. J. Siskind[55], D. A. Smith[31], F. Spada[10], G. Spandre[10], P. Spinelli[29,11], D. J. Suson[56], H. Takahashi[57], J. B. Thayer[2], D. J. Thompson[14], L. Tibaldo[2], D. F. Torres[44,58], Y. Uchiyama[35], G. Vianello[2], K. S. Wood[22], M. Wood[2], L. Zampieri[59]

[†] Corresponding author. E-mail: pierrick.martin@irap.omp.eu; lucas.guillemot@cnrs-orleans.fr; francis.e.marshall@nasa.gov

1. Deutsches Elektronen Synchrotron DESY, D-15738 Zeuthen, Germany

2. W. W. Hansen Experimental Physics Laboratory, Kavli Institute for Particle Astrophysics and Cosmology, Department of Physics and SLAC National Accelerator Laboratory,

Stanford University, Stanford, CA 94305, USA

3. Università di Pisa and Istituto Nazionale di Fisica Nucleare, Sezione di Pisa I-56127 Pisa, Italy
4. Laboratoire AIM, CEA-IRFU/CNRS/Université Paris Diderot, Service d'Astrophysique, CEA Saclay, F-91191 Gif sur Yvette, France
5. Istituto Nazionale di Fisica Nucleare, Sezione di Trieste, I-34127 Trieste, Italy
6. Dipartimento di Fisica, Università di Trieste, I-34127 Trieste, Italy
7. Department of Physics and Astronomy, University of Padova, Vicolo Osservatorio 3, I-35122 Padova, Italy
8. Istituto Nazionale di Fisica Nucleare, Sezione di Padova, I-35131 Padova, Italy
9. Dipartimento di Fisica e Astronomia "G. Galilei", Università di Padova, I-35131 Padova, Italy
10. Istituto Nazionale di Fisica Nucleare, Sezione di Pisa, I-56127 Pisa, Italy
11. Istituto Nazionale di Fisica Nucleare, Sezione di Bari, I-70126 Bari, Italy
12. Istituto Nazionale di Fisica Nucleare, Sezione di Torino, I-10125 Torino, Italy
13. Dipartimento di Fisica Generale "Amadeo Avogadro" , Università degli Studi di Torino, I-10125 Torino, Italy
14. NASA Goddard Space Flight Center, Greenbelt, MD 20771, USA
15. Laboratoire Univers et Particules de Montpellier, Université Montpellier, CNRS/IN2P3, Montpellier, France

16. Laboratoire Leprince-Ringuet, École polytechnique, CNRS/IN2P3, Palaiseau, France

17. Consorzio Interuniversitario per la Fisica Spaziale (CIFS), I-10133 Torino, Italy

18. INAF-Istituto di Astrofisica Spaziale e Fisica Cosmica, I-20133 Milano, Italy

19. Istituto Nazionale di Fisica Nucleare, Sezione di Perugia, I-06123 Perugia, Italy

20. Dipartimento di Fisica, Università degli Studi di Perugia, I-06123 Perugia, Italy

21. College of Science, George Mason University, Fairfax, VA 22030, resident at Naval Research Laboratory, Washington, DC 20375, USA

22. Space Science Division, Naval Research Laboratory, Washington, DC 20375-5352, USA

23. Agenzia Spaziale Italiana (ASI) Science Data Center, I-00133 Roma, Italy

24. INAF Osservatorio Astronomico di Roma, I-00040 Monte Porzio Catone (Roma), Italy

25. INAF Istituto di Radioastronomia, I-40129 Bologna, Italy

26. Dipartimento di Astronomia, Università di Bologna, I-40127 Bologna, Italy

27. Università Telematica Pegaso, Piazza Trieste e Trento, 48, I-80132 Napoli, Italy

28. Università di Udine, I-33100 Udine, Italy

29. Dipartimento di Fisica "M. Merlin" dell'Università e del Politecnico di Bari, I-70126 Bari, Italy

30. Erlangen Centre for Astroparticle Physics, D-91058 Erlangen, Germany

31. Centre d'Études Nucléaires de Bordeaux Gradignan, IN2P3/CNRS, Université Bordeaux 1, BP120, F-33175 Gradignan Cedex, France

32. Laboratoire de Physique et Chimie de l’Environnement et de l’Espace – Université d’Orléans / CNRS, F-45071 Orléans Cedex 02, France

33. Station de radioastronomie de Nançay, Observatoire de Paris, CNRS/INSU, F-18330 Nançay, France

34. NASA Postdoctoral Program Fellow, USA

35. 3-34-1 Nishi-Ikebukuro, Toshima-ku, Tokyo 171-8501, Japan

36. Department of Physics and Center for Space Sciences and Technology, University of Maryland Baltimore County, Baltimore, MD 21250, USA

37. Center for Research and Exploration in Space Science and Technology (CRESST) and NASA Goddard Space Flight Center, Greenbelt, MD 20771, USA

38. School of Physics and Astronomy, University of Southampton, Highfield, Southampton, SO17 1BJ, UK

39. Funded by a Marie Curie IOF, FP7/2007-2013 - Grant agreement no. 275861

40. CNRS, IRAP, F-31028 Toulouse cedex 4, France

41. Université de Toulouse, UPS-OMP, IRAP, Toulouse, France

42. Department of Physics, KTH Royal Institute of Technology, AlbaNova, SE-106 91 Stockholm, Sweden

43. The Oskar Klein Centre for Cosmoparticle Physics, AlbaNova, SE-106 91 Stockholm, Sweden

44. Institute of Space Sciences (IEEC-CSIC), Campus UAB, E-08193 Barcelona, Spain

45. Hiroshima Astrophysical Science Center, Hiroshima University, Higashi-Hiroshima, Hiroshima 739-8526, Japan

46. Istituto Nazionale di Fisica Nucleare, Sezione di Roma “Tor Vergata”, I-00133 Roma, Italy

47. Center for Cosmology, Physics and Astronomy Department, University of California, Irvine, CA 92697-2575, USA

48. CNR-IFN UOS Padova LUXOR, via Trasea 7, I-35131 Padova, Italy

49. Department of Information Engineering, University of Padova, Via G. Gradenigo 6/B, I-35131 Padova, Italy

50. Max-Planck-Institut für Physik, D-80805 München, Germany

51. Funded by contract FIRB-2012-RBFR12PM1F from the Italian Ministry of Education, University and Research (MIUR)

52. Institut für Astro- und Teilchenphysik and Institut für Theoretische Physik, Leopold-Franzens-Universität Innsbruck, A-6020 Innsbruck, Austria

53. Santa Cruz Institute for Particle Physics, Department of Physics and Department of Astronomy and Astrophysics, University of California at Santa Cruz, Santa Cruz, CA 95064, USA

54. Department of Physics, The University of Hong Kong, Pokfulam Road, Hong Kong, China

55. NYCB Real-Time Computing Inc., Lattingtown, NY 11560-1025, USA

56. Department of Chemistry and Physics, Purdue University Calumet, Hammond, IN 46323-2094, USA

57. Department of Physical Sciences, Hiroshima University, Higashi-Hiroshima, Hiroshima 739-8526, Japan

58. Institució Catalana de Recerca i Estudis Avançats (ICREA), Barcelona, Spain

59. INAF-Astronomical Observatory of Padova, Vicolo dell'Osservatorio 5, I-35122 Padova, Italy

Supplementary Materials for

An extremely bright gamma-ray pulsar in the Large Magellanic Cloud

The *Fermi*-LAT collaboration*

* Corresponding author. E-mail: pierrick.martin@irap.omp.eu;
lucas.guillemot@cnrs-orleans.fr; francis.e.marshall@nasa.gov

This PDF file includes:

S1 Materials and Methods

S1.1 Large Area Telescope data analysis

The complete LMC emission model was determined using a maximum-likelihood model-fitting approach. Typically, a model consists of several emission components and has a certain number of free parameters. A distribution of expected counts in position and energy is obtained by convolution of the model with the instrument response functions, which includes the energy-dependent point spread function, taking into account the exposure achieved for the data set that is used. Free parameters are adjusted in an iterative way until the distribution of expected counts provides the highest likelihood of the data given the model.

A complete spatial and spectral emission model for the $10^\circ \times 10^\circ$ region encompassing the LMC was derived from 73 months of *Fermi*-LAT Pass 7 Reprocessed data (*27*). The LMC model consists of a large-scale extended component spanning about the angular size of the galaxy, three smaller-scale extended components with sizes of order 1–2°, and four point sources. Two possibilities were considered for the modelling of extended emission from the LMC: 2D Gaussian gamma-ray intensity distributions, and a physical model in which emission arises from the interaction of localized populations of cosmic rays with interstellar gas. The latter option provides the model with the highest likelihood and satisfactory residuals after subtraction of the model from the data.

Based on this emission model, the spectral properties of the various sources in the LMC were updated with 75 months of Pass 8 data, using a preliminary internal version of the data and the corresponding instrumental response functions. As for the Pass 7 Reprocessed data analysis, we considered events of the so-called ‘Source’ class (as recommended by the *Fermi*-LAT collaboration for the analysis of point sources and Galactic diffuse emission), with reconstructed energies in the 0.2–100 GeV range. All event types of the SOURCE class were included: conversion in the front and back sections of the tracker, and all qualities of reconstructed energy and direction. We focus below on the two sources that are the main point of the article.

Using the whole set of Pass 8 data, PSR J0540$-$6919 is detected with a test statistic of 307 (for the definition of the test statistic, see (*41*)), corresponding to a detection at the 17σ confidence level for 3 degrees of freedom (the spectral parameters of the power law with exponential cutoff model). While significant pulsations were already detected with Pass 7 reprocessed data, using Pass 8 data resulted in an increase of nearly 2σ in the significance of the pulsations. This results primarily from the $\sim 25\%$ increase in acceptance at 1–10 GeV energies.

Restricting the analysis to the time interval over which we have a valid rotation ephemeris for PSR J0540$-$6919 (see below), we have performed a phase-resolved study by splitting the rotation period into two phase intervals, on-pulse and off-pulse, the latter being conservatively defined as the 0.3–0.8 phase range. In the on-pulse interval, PSR J0540$-$6919 is detected at the 11σ level and its spectrum can be described as a power law with photon index 2.0 ± 0.2 and an exponential cutoff at 5.2 ± 2.1 GeV. In the off-pulse interval, PSR J0540$-$6919 is detected at the 4.7σ level, and its spectrum can be described as a simple power law with photon index 2.5 ± 0.1 (while being consistent with the power-law with exponential cutoff models of the on-pulse interval and full data set). The corresponding spectra are presented in Fig. S1.

Using Pass 8 data, the source coincident with PSR J0537$-$6910 is detected with a test statistic of 127, corresponding to a 11σ detection for 4 degrees of freedom (the spectral parameters of the power law model and the position parameters). The spectrum of the source can be described as a simple power law with photon index 2.1 ± 0.1, which is consistent with the results obtained from the analysis of Pass 7 reprocessed data (*27*). Such a flat spectrum with significant emission above 20 GeV is not typical of young pulsars and may result from the superposition of weakly modulated pulsar emission with radiation from the associated pulsar wind nebula and/or supernova remnant. The energy flux above 100 MeV is $h = (1.4 \pm 0.2) \times 10^{-11}$ erg cm^{-2} s^{-1}.

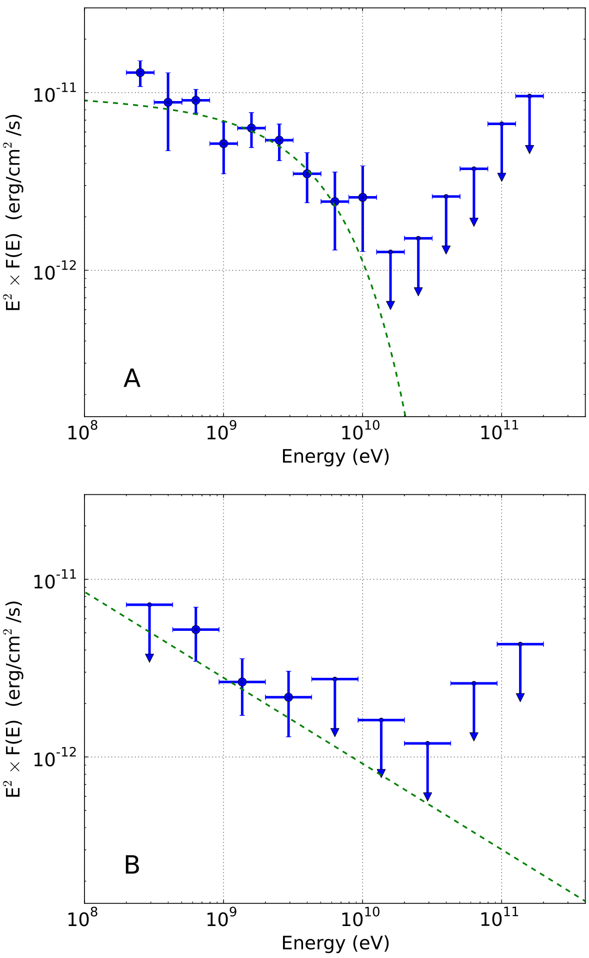

Figure S1: **Phase-resolved gamma-ray spectra of PSR J0540−6919.** (A) On-pulse phase interval. (B) Off-pulse phase interval. Upper limits correspond to a 95% confidence level. The dashed green lines show the best-fit models.

For the determination of an upper limit on the pulsed emission from PSR J0537−6910, we also quote the energy flux between 100 MeV and 10 GeV, $h = (1.1 \pm 0.2) \times 10^{-11}\,\mathrm{erg\,cm^{-2}\,s^{-1}}$.

S1.2 Rotation ephemerides for PSR J0540−6919 and PSR J0537−6910

The *Fermi* Large Area Telescope (LAT) gamma-ray data and the Iqueye photometer optical data considered in our study were phase-folded with a rotation ephemeris for PSR J0540−6919 based on Rossi X-ray Timing Explorer (RXTE) observations recorded between MJD 54602 (2008 May 16) and 55898 (2011 December 3). The solution uses the optical pulsar position, $\alpha_{\rm J2000}$ = 05^{h}40^{m}11.202^s and $\delta_{\rm J2000}$ = $-69°19'54.17''$ (*29*), and models the period and period derivative in intervals separated by two small discontinuities at MJDs 54966.4 and 55487.3 added to account for the data adequately. The resulting timing model predicts arrival times to 0.7 ms or 0.014 in pulsar phase. The timing parameters are listed in Table S1.

RXTE observations also provide an accurate ephemeris for PSR J0537$-$6910 valid from MJD 54774 (4 November 2008) to 55701 (20 May 2011), using the pulsar X-ray position $\alpha_{\rm J2000}$ = 05^{h}37^{m}47.36^s, and $\delta_{\rm J2000}$ = $-69°10'20.4''$ (*42*). Similarly to PSR J0540$-$6919, the solution models the period in intervals separated by small discontinuities. The timing model predicts arrival times to an accuracy of 0.2 ms or 0.014 in pulsar phase. The solution is given in Table S2.

S1.3 Upper limit on the pulsed luminosity of PSR J0537$-$6910

Analysis of the LAT data revealed a significant gamma-ray source at a position coincident with PSR J0537$-$6910. Its spectrum is consistent with a simple power law extending to about 50 GeV without evidence for a cutoff characteristic of pulsar magnetospheric emission. We nevertheless searched for pulsations from PSR J0537$-$6910 and failed to detect any pulsed signal with significance larger than 1σ, suggesting that strongly pulsed emission is at most a small fraction of the total signal from the source.

In order to determine an upper limit on the pulsed luminosity of PSR J0537$-$6910, we selected LAT photons found within 5° of the pulsar and having energies 0.1–10 GeV, and we assigned these photons probabilities that they originated from PSR J0537$-$6910, based on the emission model for the LMC. A Monte Carlo analysis was then performed in which for 100 logarithmically-spaced values of the pulsed fraction $p_{\rm frac}$ (where $p_{\rm frac}$ is the fraction of photons in the dataset contributing to the pulsed emission) between 10^{-3} and 1, we simulated 1000 realizations of a Gaussian-shaped profile for the pulsed emission containing $N_{\rm psr} = p_{\rm frac} \times N$ photons (where N denotes the total number of photons in the dataset) and $N_{\rm bkgd} = N - N_{\rm psr}$ background photons with random phases. A full width at half maximum of 10% of the pulsar rotation was used for the simulated gamma-ray profile, similar to the X-ray profile of PSR J0537$-$6910 (*11*). For each realization, $N_{\rm psr}$ values of the spectral weights were selected at random from the actual dataset, and the remaining spectral weights were randomly assigned to the other $N_{\rm bkgd}$ photons. Finally, we calculated the weighted H-test parameter at each step, and determined the fraction of $> 5\sigma$ detections among the 1000 realizations, for each $p_{\rm frac}$ value.

The conclusion from the Monte Carlo analysis was that any value of $p_{\rm frac}$ larger than ~ 0.06 results in highly significant detections in at least 95% of cases. This value of $p_{\rm frac}$ can therefore be used to place an upper limit on the pulsed luminosity of PSR J0537$-$6910. With a total 0.1–10 GeV luminosity for the source coincident with PSR J0537$-$6910 of $L_{\gamma,\ \rm J0537} = 3.1 \times 10^{36}$ erg s^{-1} (*27*), we obtain a limit of $p_{\rm frac} \times L_{\gamma,\ \rm J0537} \sim 1.9 \times 10^{35}$ erg s^{-1}.

Parameter	Value
Right Ascension, α_{J2000}	05^{h}40^{m}11.202^s
Declination, δ_{J2000}	$-69°19'54.17''$
Reference Epoch (MJD)	54792.81555049109
Spin Frequency, ν (Hz)	19.74426902754
First Time Derivative of ν, $\dot{\nu}$ (10^{-10} Hz s^{-1})	-1.8667600
Second Time Derivative of ν, $\ddot{\nu}$ (10^{-21} Hz s^{-2})	3.7502
Epoch of Discontinuity 1 (MJD)	54966.4266616022
Increment in Rotational Phase	0.005
Increment in ν (Hz)	-0.56×10^{-8}
Increment in $\dot{\nu}$ (10^{-10} Hz s^{-1})	2×10^{-6}
Increment in $\ddot{\nu}$ (10^{-21} Hz s^{-2})	0.054
Epoch of Discontinuity 2 (MJD)	55487.25999493553
Increment in Rotational Phase	0.010
Increment in ν (Hz)	-1.96×10^{-8}
Increment in $\dot{\nu}$ (10^{-10} Hz s^{-1})	2.74×10^{-5}
Increment in $\ddot{\nu}$ (10^{-21} Hz s^{-2})	-0.283
Solar System Ephemeris	DE200
Reference Time Scale	TDB
Validity Range (MJD)	54602 – 55898
RMS Timing Residuals (ms)	0.7

Table S1: Timing parameters for PSR J0540−6919.

Parameter	Value
Right Ascension, α_{J2000}	05^{h}37^{m}47.36^s
Declination, δ_{J2000}	$-69°10'20.4''$
Reference Epoch (MJD)	54677.07480975035
Spin Frequency, ν (Hz)	61.9815193952
First Time Derivative of ν, $\dot{\nu}$ (10^{-10} Hz s^{-1})	-1.994664
Second Time Derivative of ν, $\ddot{\nu}$ (10^{-21} Hz s^{-2})	9.6
Epoch of Discontinuity 1 (MJD)	54711.79703197257
Increment in Rotational Phase	0.090
Increment in ν (Hz)	6.5921×10^{-6}
Increment in $\dot{\nu}$ (10^{-10} Hz s^{-1})	-0.716×10^{-3}
Epoch of Discontinuity 2 (MJD)	54769.66740234294
Increment in Rotational Phase	0.696
Increment in ν (Hz)	22.4152×10^{-6}

Continued on next page

Parameter	Value
Increment in $\dot{\nu}$ (10^{-10} Hz s^{-1})	-0.846×10^{-3}
Epoch of Discontinuity 3 (MJD)	54885.40814308368
Increment in Rotational Phase	0.741
Increment in ν (Hz)	21.2181×10^{-6}
Increment in $\dot{\nu}$ (10^{-10} Hz s^{-1})	-1.004×10^{-3}
Epoch of Discontinuity 4 (MJD)	55041.65814308368
Increment in Rotational Phase	0.378
Increment in ν (Hz)	13.4614×10^{-6}
Increment in $\dot{\nu}$ (10^{-10} Hz s^{-1})	-1.563×10^{-3}
Increment in $\ddot{\nu}$ (10^{-21} Hz s^{-2})	11.3
Epoch of Discontinuity 5 (MJD)	55182.86184678738
Increment in Rotational Phase	0.582
Increment in ν (Hz)	13.0182×10^{-6}
Increment in $\dot{\nu}$ (10^{-10} Hz s^{-1})	-2.6679×10^{-3}
Epoch of Discontinuity 6 (MJD)	55267.35258752813
Increment in Rotational Phase	0.300
Increment in ν (Hz)	34.0678×10^{-6}
Increment in $\dot{\nu}$ (10^{-10} Hz s^{-1})	-1.241×10^{-3}
Increment in $\ddot{\nu}$ (10^{-21} Hz s^{-2})	-14.17
Epoch of Discontinuity 7 (MJD)	55452.53777271331
Increment in Rotational Phase	0.643
Increment in ν (Hz)	10.4278×10^{-6}
Increment in $\dot{\nu}$ (10^{-10} Hz s^{-1})	-0.867×10^{-3}
Epoch of Discontinuity 8 (MJD)	55452.53777271331
Increment in Rotational Phase	0.900
Increment in ν (Hz)	7.6476×10^{-6}
Increment in $\dot{\nu}$ (10^{-10} Hz s^{-1})	-0.420×10^{-3}
Epoch of Discontinuity 9 (MJD)	55556.70443937997
Increment in Rotational Phase	0.122
Increment in ν (Hz)	0.6292×10^{-6}
Increment in $\dot{\nu}$ (10^{-10} Hz s^{-1})	0.730×10^{-3}
Epoch of Discontinuity 10 (MJD)	55585.639624565163
Increment in Rotational Phase	0.027
Increment in ν (Hz)	5.4499×10^{-6}
Increment in $\dot{\nu}$ (10^{-10} Hz s^{-1})	-1.800×10^{-3}
Epoch of Discontinuity 11 (MJD)	55614.574809750346
Increment in Rotational Phase	0.156
Increment in ν (Hz)	28.1097×10^{-6}

Continued on next page

Parameter	Value
Increment in $\dot{\nu}$ (10^{-10} Hz s^{-1})	0.057×10^{-3}
Solar System Ephemeris	DE200
Reference Time Scale	TDB
Validity Range (MJD)	54774 – 55701
RMS Timing Residuals (ms)	0.2

Table S2: Timing parameters for PSR J0537$-$6910.